Bart Eggen

Tomography of Dynamical Systems

Bachelor thesis

June 30, 2017

Thesis supervisors: **Prof.dr. K.J. Batenburg**
                            Dr. H.J. Hupkes
                            Prof.dr. K.H. Kuijken

Leiden University
Mathematical Institute

Contents

1   Introduction

The goal of tomography is to obtain an image of the interior of an object, by only using projections of it. This image is called a reconstruction, as it is an inverse process. However, when the object moves during the projection measurements, the reconstructed image will become blurry. Numeral solutions to the correction of dynamics already have been found, for example in fluid dynamics [1]. In this thesis, a method is described to correct simple dynamics as well as rotational dynamics directly in the obtained data.

Another remarkable application of tomography is in astronomy [2]. It uses the rotation of certain systems to obtain projections from different angles. One problem that arises is that these systems are not directly observable. They are distant and the resolution of current telescopes is not good enough to resolve them. There are however ways to obtain information about them. One method used is spectroscopy, which measures the amount of light coming from the source at specific wavelengths. Because the system rotates, some parts move away from earth while others move towards it. This causes Doppler shifts in the light and this can be seen on spectroscopic data if one knows the exact wavelength at which the light was emitted. These spectroscopic measurements can be taken relatively quick and therefore if one spreads out the measurements over time, the data gathered will be coming from different angles of the system. It is on this data that tomography can be applied. In this thesis, the reason why this is possible will be explained. Specific systems called Cataclysmic Variable stars are modelled in different ways and the data that would be obtained from these systems is simulated. Also the data is simulated, obtained from these systems when extra rotational dynamics is added. This thesis also proposes a method of directly cancelling out these dynamics in the data, so a proper reconstruction can be made. The final chapter describes a method to reconstruct spectroscopic data that overlaps. However, it will start with an introduction about tomography and how it can be applied.

2   Tomography

In this section, part of the theoretical background behind tomography will be discussed. This will be done analytically as well as with linear algebra. The chapter starts with the famous Radon transform and continues by using Fourier analysis to find some analytical inversion methods that are used in imaging today. Only the two dimensional case will be explained, but the theory can be extended to more dimensions by using more general properties in linear algebra and calculus [3]. At the end of the section, the algebraic theory will be discussed that leads to some other reconstruction methods.

For the creation of certain images and the application of the theory, the ASTRA Toolbox is used [4, 5].

2.1   The Radon Transform

The Radon transform is an analytical way to describe projections of objects. First a definition and some notation are needed to understand how these words are connected to mathematics.

Definition 2.1.1. *An* object *is a function* $f : \mathbb{R}^2 \to \mathbb{R}$ *with* $f \in \mathcal{S}(\mathbb{R}^2)$, *where* $\mathcal{S}(\mathbb{R}^2)$ *is the Schwartz space on* $\mathbb{R}^2$. *This means that for every multi index* $\alpha, \beta \in \mathbb{Z}_+^2$ *the following inequality holds*

$$\sup_{\mathbf{x} \in \mathbb{R}^2} |\mathbf{x}^\alpha \partial^\beta f(\mathbf{x})| < \infty. \tag{1}$$

For more information about multi indices and this particular notation, one should read chapter 1 of [6]. The Schwartz space is the space of functions that are rapidly decreasing. The definition ensures that objects behave nicely when applying the Fourier transform, which is needed in the following chapter. Also, it is a sufficient condition for the Radon transform to be applied. The transform integrates over lines under certain angles to obtain projections. These lines can be described in the following way

$$L(\theta, \rho) = \{(x, y) \in \mathbb{R}^2 : x \cos(\theta) + y \sin(\theta) = \rho\} \tag{2}$$

for $\theta \in [0, 2\pi)$ and $\rho \in \mathbb{R}$. The coordinate θ changes the angle of the line, while the coordinate ρ is the position where the line crosses the two dimensional plane rotated under the angle θ. In figure 1 it can be seen how such a line changes when θ and ρ are changed.

With the previous, the Radon transform can be defined.

Definition 2.1.2 (Radon transformation)**.** *The* Radon transform *of an object* f *along a line* $L(\theta, \rho)$ *is the map* $\mathcal{R}(f)$ *defined by*

$$(\mathcal{R}f)(\theta, \rho) = \int_{L(\theta,\rho)} f(x, y)dxdy = \int_{-\infty}^{\infty} \int_{-\infty}^{\infty} f(x, y)\delta(x \cos(\theta) + y \sin(\theta) - \rho)dxdy \tag{3}$$

where δ *is the Dirac delta function.*

The definition introduces the Dirac delta function as to simplify the region over which is integrated.

For a specific $\theta \in [0, 2\pi)$, the Radon transform gives a one dimensional function $(\mathcal{R}f)_\theta(\rho) := (\mathcal{R}f)(\theta, \rho)$. Such a function is called a projection under angle θ. In figure 1 it can be seen how such a projection is visualized. Combining projections under multiple angles, gives a so called sinogram. A sinogram has an interesting property, namely that for $\theta \in [0, \pi)$, the projection
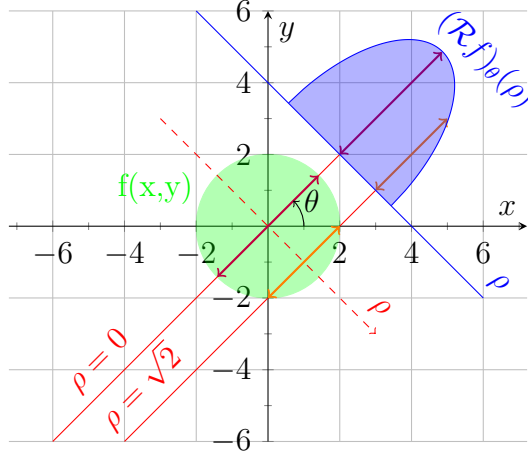
Figure 1: In this example, the object f is a constant function on a circle with radius 2. Projections are taken from an angle θ. The lines along which is integrated are shown in red. Two lines with different ρ are plotted. The integration along such a red line results in a certain value as shown in purple and yellow. These are the arrows in the object and in the blue graph. Combining the values of integration for different ρ at the same angle θ, a projection under angle θ is obtained as shown in blue.

under angle $\theta + \pi$ is exactly mirrored around $\rho = 0$. This follows from the definition of the lines along which is integrated.

$$L(\theta + \pi, \rho) = \{(x, y) \in \mathbb{R}^2 : x\cos(\theta + \pi) + y\sin(\theta + \pi) = \rho\} \tag{4}$$
$$= \{(x, y) \in \mathbb{R}^2 : -x\cos(\theta) - y\sin(\theta) = \rho\} \tag{5}$$
$$= \{(x, y) \in \mathbb{R}^2 : x\cos(\theta) + y\sin(\theta) = -\rho\} \tag{6}$$
$$= L(\theta, -\rho) \tag{7}$$

This property makes it sufficient in practice to only obtain projections under angles $\theta \in [0, \pi)$. An example of a sinogram can be seen in figure 2.

In this case, the lines along which is integrated for a projection are parallel lines. That is why this type of projection is called a parallel projection. An example of another type of projection is the fan beam projection, where all lines are coming from a specific source (this is used in CT-imaging). However this will not be relevant for this thesis so only parallel projections are focussed on.

2.2   Fourier Slice Theorem

In the previous chapter the Radon transform was defined. In this chapter a method is discussed that is an inversion of this transform. As the name of the chapter contains the word Fourier, it is only logical to introduce the following notation.

Definition 2.2.1. *Let f be an object, the* Fourier transform $\hat{f}$ *of f is defined as*

$$\hat{f}(u, v) = \int_{-\infty}^{\infty} \int_{-\infty}^{\infty} f(x, y) e^{-2\pi i(xu + yv)} dx dy. \tag{8}$$

This is a convention, there are also other ways to define the Fourier transform of an object. A nice property of functions in the Schwartz space, is that the Fourier transform maps again to the Schwartz space. Therefore the following theorem holds [7, p. 182]
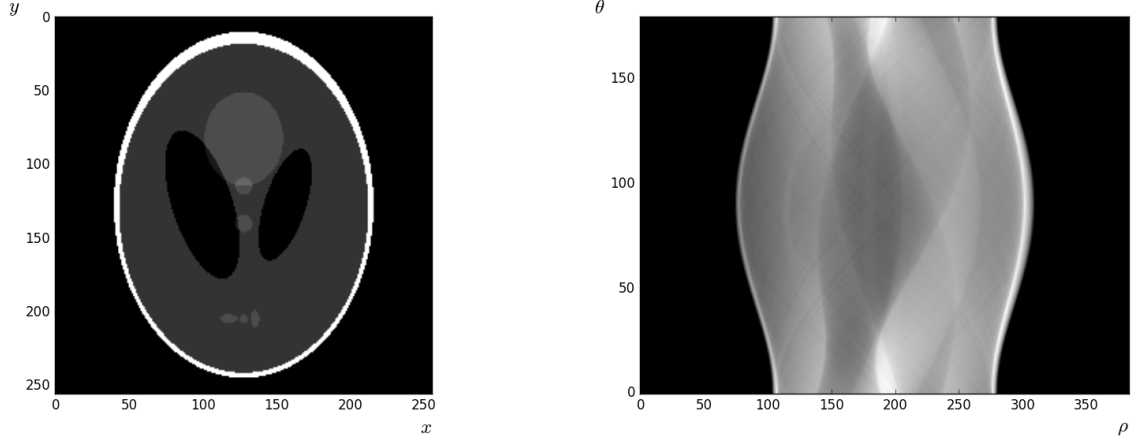
Figure 2: The left image is the object. It is called the Shepp-Logan phantom. This object was created with the purpose of simulating a human head and is used in the testing of reconstruction algorithms. The grey scale indicates the function value of f, where light indicates a high value of f and dark indicates a low value. When projections are taken under multiple angles one obtains the sinogram on the right.

Theorem 2.2.1 (Inverse Fourier Theorem). *Let f be an object, then the following equality holds for all $(x, y) \in \mathbb{R}^2$*

$$f(x, y) = \int_{-\infty}^{\infty} \int_{-\infty}^{\infty} \hat{f}(u, v) e^{2\pi i(xu+yv)} du dv \tag{9}$$

$\square$

Note that such a function can be Fourier transformed over only one coordinate. Take for example a projection under an angle θ. This is a one dimensional function and the Fourier transform of this function will be denoted by

$$\widehat{(\mathcal{R}f)}_\theta(r) = \int_{-\infty}^{\infty} (\mathcal{R}f)(\theta, \rho) e^{-2\pi i r \rho} d\rho. \tag{10}$$

Fourier transforms are a useful tool. If one would be able to find the Fourier transformed object, a simple inverse Fourier transform is enough to obtain a reconstruction of the original object. This is exactly what happens in the following theorem.

Theorem 2.2.2 (Fourier slice theorem). *Let f be an object, and suppose a projection under angle θ is obtained. Then the following equality holds*

$$\widehat{(\mathcal{R}f)}_\theta(r) = \hat{f}(r\cos(\theta), r\sin(\theta)) \tag{11}$$

Proof. The proof is relatively easy, as it is just rewriting things.

$$\widehat{(\mathcal{R}f)}_\theta(r) = \int_{-\infty}^{\infty} (\mathcal{R}f)(\theta, \rho) e^{-2\pi i r \rho} d\rho$$

$$= \int_{-\infty}^{\infty} \int_{-\infty}^{\infty} \int_{-\infty}^{\infty} f(x, y) \delta(x\cos(\theta) + y\sin(\theta) - \rho) e^{-2\pi i r \rho} dx dy d\rho$$

$$= \int_{-\infty}^{\infty} \int_{-\infty}^{\infty} f(x, y) \left(\int_{-\infty}^{\infty} \delta(x\cos(\theta) + y\sin(\theta) - \rho) e^{-2\pi i r \rho} d\rho \right) dx dy$$

6

where it is used that $f(x,y)$ does not depend on ρ. The Dirac delta function is 0 everywhere except when $\rho = x\cos(\theta) + y\sin(\theta)$, so by using this the following is obtained.

$$
\begin{aligned}
\widehat{(\mathcal{R}f)}_\theta(r) &= \int_{-\infty}^{\infty}\int_{-\infty}^{\infty} f(x,y)\left(\int_{-\infty}^{\infty} \delta(x\cos(\theta) + y\sin(\theta) - \rho)e^{-2\pi ir\rho}d\rho\right)dxdy \\
&= \int_{-\infty}^{\infty}\int_{-\infty}^{\infty} f(x,y)e^{-2\pi ir(x\cos(\theta)+y\sin(\theta))}dxdy \\
&= \int_{-\infty}^{\infty}\int_{-\infty}^{\infty} f(x,y)e^{-2\pi i(r\cos(\theta)x+r\sin(\theta)y)}dxdy \\
&= \hat{f}(r\cos(\theta), r\sin(\theta)).
\end{aligned}
$$

$\square$

One can also directly see why this theorem is called the slice theorem. By Fourier transforming a projection of the object under a fixed angle we receive a line (or a so called slice) in the Fourier domain of the object. If more projections are added over different angles, the whole Fourier domain of the object will eventually be filled, as can be seen in figure 3. The original object can then be found by using the inverse Fourier transform.

This theorem gives a method to reconstruct the object, when only projections of the object are known. The only problem with this method is that it is often not useful in practice [8]. The Fast Fourier Transform uses Cartesian coordinates, while in this case the data is obtained in polar coordinates as can be seen in figure 3. Therefore a computer first needs to interpolate the values to Cartesian coordinates, which reduces accuracy of the reconstruction.

So it is desirable to find a way that is both computationally efficient and accurate. Luckily, there is one and it is called the filtered back projection (FBP).
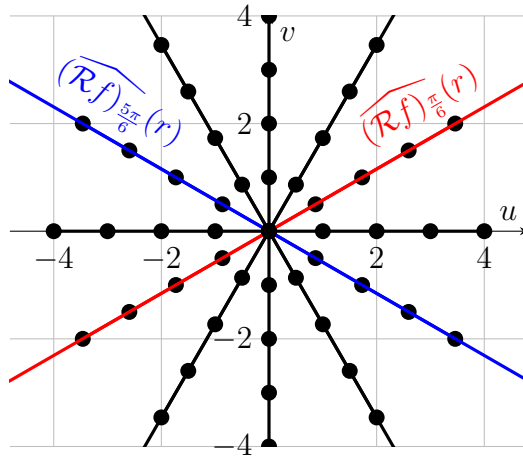

Figure 3: Some slices can be seen under different angles. In red the slice at angle $\theta = \frac{\pi}{6}$ and in blue the slice at angle $\theta = \frac{5\pi}{6}$. Suppose one can only obtain projections at discrete points. The circles indicate how evenly spread data points lie in the Fourier domain. This way it can be seen that for higher (lower) frequencies, the data points are under (over) represented as there is more (less) space between neighbouring data points. This illustrates why the filter $|r|$ is being used in the Fourier domain of a projection in the filtered back projection.

2.3 Filtered Back Projection

The filtered back projection is the most commonly used analytical inversion method in tomography. First, the theorem will be proved and then it will be explained.

Theorem 2.3.1 (Filtered Back Projection). *Let $(x, y) \in \mathbb{R}^2$. Let f be an object and suppose projections are taken under all angles $\theta \in [0, \pi)$ along the lines $\rho = x \cos(\theta) + y \sin(\theta)$. Then the following equality holds,*

$$f(x, y) = \int_0^\pi \int_{-\infty}^\infty \widehat{(\mathcal{R}f)}_\theta(r) e^{2\pi i r \rho} |r| \, dr \, d\theta. \tag{12}$$

Proof. The main trick used in this proof is changing to polar coordinates in the Fourier domain. The reason why this is done follows from the Fourier slice theorem, in which the Fourier transformed object f uses these coordinates. First, the inverse Fourier transform is taken and then the coordinate change is applied, with the integration factor r.

$$\begin{aligned}
f(x, y) &= \int_{-\infty}^\infty \int_{-\infty}^\infty \hat{f}(u, v) e^{2\pi i (xu + yv)} \, du \, dv \\
&= \int_0^{2\pi} \int_0^\infty \hat{f}(r \cos(\theta), r \sin(\theta)) e^{2\pi i (xr \cos(\theta) + yr \sin(\theta))} r \, dr \, d\theta \\
&= \int_0^\pi \int_0^\infty \hat{f}(r \cos(\theta), r \sin(\theta)) e^{2\pi i (xr \cos(\theta) + yr \sin(\theta))} r \, dr \, d\theta \\
&\quad + \int_0^\pi \int_0^\infty \hat{f}(r \cos(\theta + \pi), r \sin(\theta + \pi)) e^{2\pi i (xr \cos(\theta + \pi) + yr \sin(\theta + \pi))} r \, dr \, d\theta
\end{aligned}$$

where the integral is split over θ up in two parts. Next, basic goniometric identities are used to get rid of the $+\pi$ factors and the sign of r is changed by using a substitution. By doing this, the two parts can be added back together again.

$$\begin{aligned}
f(x, y) &= \int_0^\pi \int_0^\infty \hat{f}(r \cos(\theta), r \sin(\theta)) e^{2\pi i (xr \cos(\theta) + yr \sin(\theta))} r \, dr \, d\theta \\
&\quad + \int_0^\pi \int_0^\infty \hat{f}(-r \cos(\theta), -r \sin(\theta)) e^{2\pi i (-xr \cos(\theta) - yr \sin(\theta))} r \, dr \, d\theta \\
&= \int_0^\pi \int_0^\infty \hat{f}(r \cos(\theta), r \sin(\theta)) e^{2\pi i (xr \cos(\theta) + yr \sin(\theta))} r \, dr \, d\theta \\
&\quad + \int_0^\pi \int_{-\infty}^0 \hat{f}(r \cos(\theta), r \sin(\theta)) e^{2\pi i (xr \cos(\theta) yr \sin(\theta))} (-r) \, dr \, d\theta \\
&= \int_0^\pi \int_{-\infty}^\infty \hat{f}(r \cos(\theta), r \sin(\theta)) e^{2\pi i (xr \cos(\theta) + yr \sin(\theta))} |r| \, dr \, d\theta
\end{aligned}$$

Now, the Fourier slice theorem and the line identity $x \cos(\theta) + y \sin(\theta) = \rho$ are used to obtain

$$\begin{aligned}
f(x, y) &= \int_0^\pi \int_{-\infty}^\infty \hat{f}(r \cos(\theta), r \sin(\theta)) e^{2\pi i (xr \cos(\theta) + yr \sin(\theta))} |r| \, dr \, d\theta \\
&= \int_0^\pi \int_{-\infty}^\infty \widehat{(\mathcal{R}f)}_\theta(r) e^{2\pi i r \rho} |r| \, dr \, d\theta.
\end{aligned}$$

$\square$

If one looks closely to the middle integral it can be seen that this is almost the inverse Fourier transform of $\widehat{(\mathcal{R}f)_\theta}$. The only factor that is strange is the $|r|$. If the factor $|r|$ is left out, the result would be

$$f(x,y)_{BP} = \int_0^\pi \int_{-\infty}^\infty \widehat{(\mathcal{R}f)}_\theta(r)e^{2\pi i r\rho} dr d\theta = \int_0^\pi (\mathcal{R}f)(\theta,\rho)d\theta. \tag{13}$$

This gives to each point (x,y) under each angle θ the value of the projection along the line $x\cos(\theta) + y\sin(\theta)$ and adds all these values from all different angles. So this 'smears' out the object as the value of the projection is also assigned to places where there is no object. This is called a back projection. Even if one would use a lot of projections, this image will always look a bit blurry as can be seen in 4. So why does the factor $|r|$ fix this blurriness? This can be understood by looking at figure 3. One can see that at the low values of u and v, there are more points closely together than at bigger values. This is because of the slices in the Fourier domain. So in some way, the lower frequencies are over represented. The factor $|r|$ now makes sure that the higher frequencies get a bigger 'weight' in the integral so that all frequencies are represented equally. This factor $|r|$ is called the *Ram-Lak* filter. This is also the reason why it is called a filtered back projection, it is a back-projection but with a 'filter' applied in the Fourier domain. In practice, when there is noise in the image, the Ram-Lak filter could also amplify these errors. That is why different filters are sometimes used in the back projection.

The filtered back projection is a useful tool in computational tomography, as computers can calculate these values fairly easy and quick. However there are also downsides to this method. First of all it requires a lot of projections to be accurate and you need the full angular range. Also, the outcome is highly affected by noise, which makes it less useful in some scenarios [8].

2.4 Algebraic Tomography

In this chapter the algebraic tomographic model is introduced. The set-up used is the same as in [1]. First, the object has to be defined. This is done by putting a grid with a total of N pixels on top of the item one wants to reconstruct. These pixels are ordered and all have an index $j \in \{1,\cdots,N\}$. It is assumed that in each pixel, the item has a constant value. Using these conventions, the object can be defined as follows

Definition 2.4.1. *A discrete object is a column vector* $\mathbf{x} = (x_1,\cdots,x_N) \in \mathbb{R}^n$, *where the component* x_j *for* $j \in \{1,\cdots,N\}$ *are the values of the item at pixel* j.

Just as in the analytical case, object values are summed over straight lines. But because the lines do not overlap a certain pixel as much as another, weights are introduced for every pixel. These weights are defined as the length of the lines through a pixel. This can be seen in figure 5 and the following definition can be given

Definition 2.4.2. *Let* M *be the amount of lines over which the object values are summed. The collection of weights is the matrix* $\mathbf{W} \in \mathbb{R}^{M \times N}$, *where for* $i \in \{1,\cdots,M\}$ *and* $j \in \{1,\cdots,N\}$ *the element* w_{ij} *is the weight of line* i *through pixel* j. *This weight can be taken as the length of the line through pixel* j.

These lines are called projection lines and all lines combined with the same angle are called a projection. The following definition mathematically states what projections are based on the previous definitions.

Definition 2.4.3. *The* projection data *is the column vector* $\mathbf{p} = (p_1,\cdots,p_M) \in \mathbb{R}^M$ *consisting of measured samples of the Radon transform of the object, where each element* p_i *corresponds to a particular line through the object. This can also be written as*

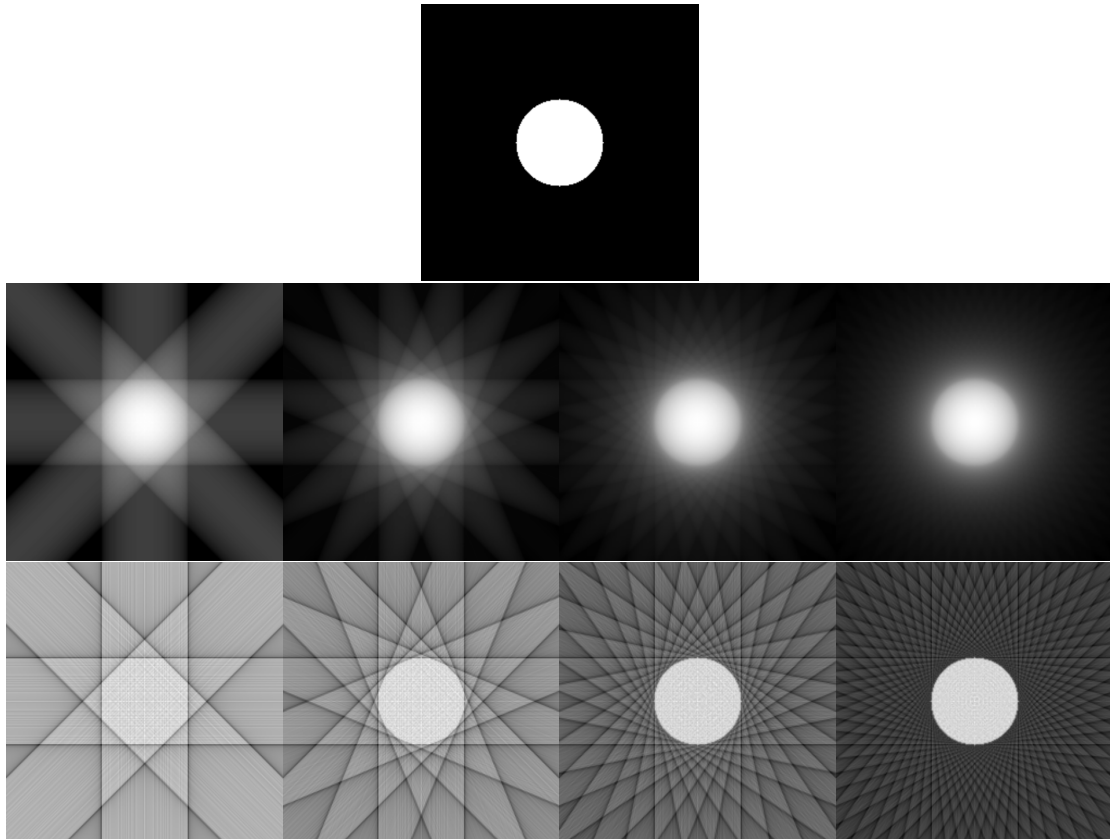$$\mathbf{p} = \mathbf{W} \cdot \mathbf{x} \tag{14}$$

Figure 4: The to be reconstructed object is a constant circle shaped function. The first row is reconstructed using only the back projection and the last row is reconstructed using the filtered back projection. The first column is a reconstruction with 4 projections, the second column with 8, the third with 16 and the last with 32. Although the back projection reconstructions look better in comparison to the original in figure 4, it only seems that way. In fact, the filtered back projection performs a lot better. In chapter 2.6, a measure will be introduced to support this claim.

A projected line will only go through a few pixels in comparison to the total amount of pixels, so the matrix $\mathbf{W}$ is usually sparse. This set-up can be seen in figure 5.

The problem of reconstruction now comes down to solving the following system of linear equations for $\mathbf{x}$

$$\mathbf{W}\mathbf{x} = \mathbf{p}. \tag{15}$$

Most of the time, the projections are known and the object has to be reconstructed. This comes down to solving the linear equations in 15. Note that the values for N and M are usually big and make direct solving of these equations almost impossible. Also, when $M < N$, there are less equations than variables and therefore the system is under determined. This makes solutions that are found not unique. When $M > N$, the system is overdetermined and in general does not have a solution. There are many algorithms that approximate the solution of the system in equation 15. Most of these come down to minimizing $||\mathbf{W}\mathbf{x} - \mathbf{p}||$ as a function of $\mathbf{x}$ for a certain norm $|| \cdot ||$. In the next chapter, an example of such a reconstruction algorithm will be given.
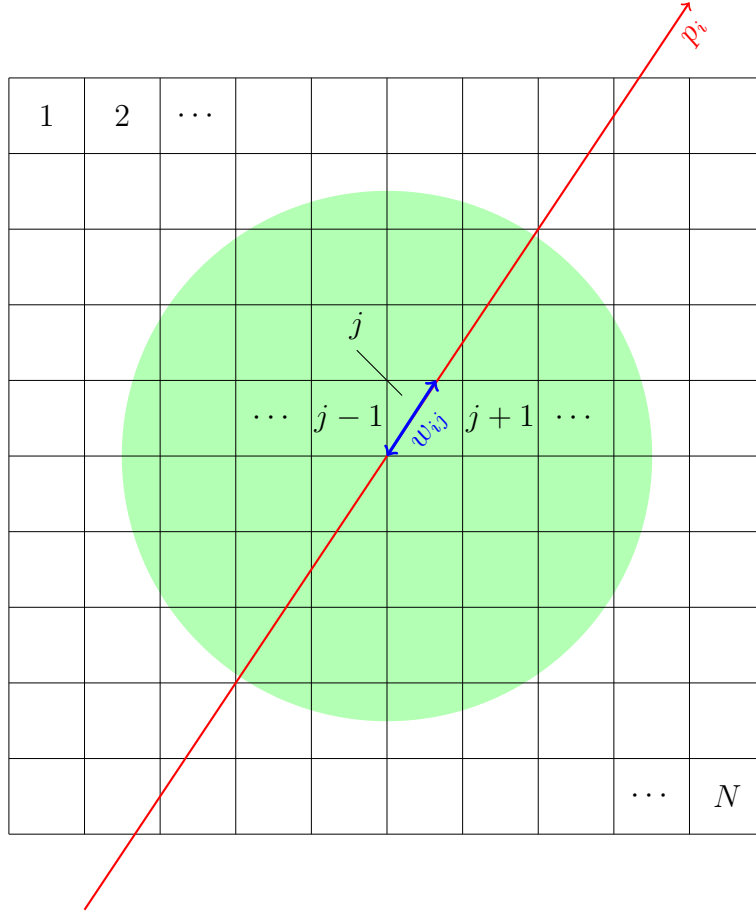
Figure 5: The algebraic set-up for tomography.The object is discretized and represented on a grid with a total of N pixels. Projections can be seen as summations along straight lines, where the length of the line in each pixel gives the weight of the object value through that pixel.

2.5 SIRT

A widely used algebraic reconstruction algorithm is Simultaneous Iterative Reconstruction Technique (SIRT). This uses a starting solution for $\mathbf{x}$ (usually the zero vector) and updates this solution every step based on the projections and the weight matrix. In the i-th iteration, the update is given by

$$\mathbf{x}^{(i)} = \mathbf{x}^{(i-1)} + \mathbf{C}\mathbf{W}^{\mathbf{T}}\mathbf{R}(\mathbf{p} - \mathbf{W}\mathbf{x}^{(i-1)}) \tag{16}$$

where $\mathbf{x}^{(i)}$ is the i-th update of $\mathbf{x}$, $\mathbf{W}^{\mathbf{T}}$ is the transposed weight matrix, $\mathbf{C}$ is the $N \times N$ diagonal matrix with $C_{jj} = 1/\sum_i W_{ij}$ for $j \in \{1, \cdots, N\}$ and $\mathbf{R}$ is the $M \times M$ diagonal matrix with $R_{ii} = 1/\sum_j W_{ij}$ for $i \in \{1, \cdots, M\}$. So the $\mathbf{C}$ and $\mathbf{R}$ matrix contain the inverse of the column and row sums of the weight matrix respectively. The reason these matrices are needed is to compensate for the number of projection lines that hit each pixel and the amount of pixels that hit each projection line.

When the solution at every iteration gets closer to the optimal solution, then $\mathbf{W}\mathbf{x}^{(i-1)} \approx \mathbf{p}$ and the last term of the update step will become almost zero. This results in only a small update and the factor in front makes sure this update is an improvement. Eventually the iterations will get closer and closer to the optimal solution. In this thesis, most reconstructions are done using this algorithm. This is standard implemented in the ASTRA Toolbox, however in chapter 4.6 this algorithm is used manually for reasons that can be read in that chapter. In this thesis, 150 iterations are used in most reconstructions.

2.6 Reconstruction quality

There are many ways to reconstruct objects by using projections. Therefore, a method is needed to determine which reconstruction method works better in what scenario. The set-up from chapter 2.4 is used. This does not mean that this measure does not exist for the analytical set-up. In practice however, the algebraic set-up is used as detectors always contain a finite amount of pixels. Solving the linear equations in 15 gives a reconstructed object. The following measure is defined on this image.

Definition 2.6.1. *Let* $\mathbf{x}$ *be a discrete object that is unequal to zero and* $\tilde{\mathbf{x}}$ *the reconstructed object, the* Relative Root Mean Squared Error (RRMSE) *is defined as*

$$RRMSE(\tilde{\mathbf{x}}) = \sqrt{\frac{\sum_{j=1}^{N}(x_j - \tilde{x}_j)^2}{\sum_{j=1}^{N} x_j^2}} \tag{17}$$

The RRMSE will be closer to 0 when the reconstruction is better. As an example, table 1 shows the RRMSE values for the reconstructions in figure 4.

	4 projections	8 projections	16 projections	32 projections
BP	154.9	150.9	150.6	150.6
FBP	1.512	0.8793	0.5059	0.2847

Table 1: RRMSE calculations of the images in figure 4. The high values in the backprojected images are due to the smearing. This causes all projections under different angles to be added, which results in really high pixel values. It can also be seen that the increase of projections drastically decreases the error.

In this table, one can also see that the RRMSE decreases when more projections are taken. However, in practice it is often not possible to take many projections. In a CT-scan, radiation is used that harms the patient, therefore the amount of projections taken should be the least amount possible while still obtaining a quality reconstruction. Different reconstruction methods can be applied to different scenarios to obtain the best results. For example, algebraic reconstruction methods often behave better when less projections are taken. If one desires that the calculations are fast, the analytical reconstruction methods are often better. There are many more possible factors that come in to play, for example the amount of noise, dynamics or that projections can only be taken in a certain interval of angles.

3 Dynamics

In this section the consequences of movement of the objects during the acquisition of he tomographic projection data will be discussed. Also a method will be given to incorporate simple movement in the calculations to compensate for these movements in the reconstruction.

3.1 Simple dynamic objects

In many practical scenarios, the objects that one wants to reconstruct undergo a certain movement. In medical X-ray tomography for example, the human heart is moving periodically. While it is moving, projections are acquired. One can imagine that this results in a blurry reconstruction, as the heart is in a different place for different projections. First a method to obtain the average velocity of an object in a certain time interval will be discussed.

In definition 2.1.1, an object was analytically defined. To incorporate dynamics, a slight adjustment to this definition is needed.

Definition 3.1.1. *A* moving object *is a function $g : \mathbb{R}^2 \times \mathbb{R}_{>0} \to \mathbb{R}$, such that $g(\cdot, \cdot, t)$ is an object for every $t \in \mathbb{R}_{>0}$ and $g(x, y, \cdot)$ is piecewise continuous for every $(x, y) \in \mathbb{R}^2$.*

This definition makes sure that at any time t, the moving object is an object as defined in the previous section. The piecewise continuity is not entirely necessary, but it makes sure the object does not behave too strangely. Suppose the object g moved a distance $\Delta \mathbf{r}$ in a time interval $\Delta t = t_1 - t_0$, the average velocity is then calculated by

$$\mathbf{v}_{\text{avg}} = (v_x, v_y) = \frac{\Delta \mathbf{r}}{\Delta t} \tag{18}$$

From now on, $t_1 = t$ and $t_0 = 0$, so that $\Delta t = t$. For the calculation of the average velocity, one needs to know how much the object has moved between each time step. A simple method to determine this, is by calculating the center of mass of the object each time step. First of all, it is assumed that the object is a connected shape, maintains its shape during the movement and does not rotate. This assumption gives rise to the following equation

$$g(x, y, t) = f(x - v_x \cdot t, y - v_y \cdot t), \tag{19}$$

where the stationary object f is the moving object g at $t = 0$. Let g be a moving object, the center of mass at time t will then be given by

$$\mathbf{R}(t) = (R_x(t), R_y(t)) = \frac{\int_{-\infty}^{\infty} \int_{-\infty}^{\infty} g(x, y, t) \cdot \mathbf{r} dx dy}{\int_{-\infty}^{\infty} \int_{-\infty}^{\infty} g(x, y, t) dx dy}, \tag{20}$$

where $\mathbf{r} = (x, y)$ is the vector with the position. Naturally this can be written as a discrete center of mass by taking the sum instead of the integral. The average velocity in a time interval $\Delta t = t$ will then be given by

$$\mathbf{v}_{\text{avg}} = \frac{\mathbf{R}(t) - \mathbf{R}(0)}{t}. \tag{21}$$

This result can be used if the complete moving object g can be reconstructed, but in practice this is not possible. Luckily, a complete reconstruction of the object is not needed. In fact, only two projections under different angles are necessary to find the center of mass of the moving object at time t.

This can be understood by thinking about how projection are constructed. When a projection under angle θ is taken of an object, the center of mass is also projected on that projection.
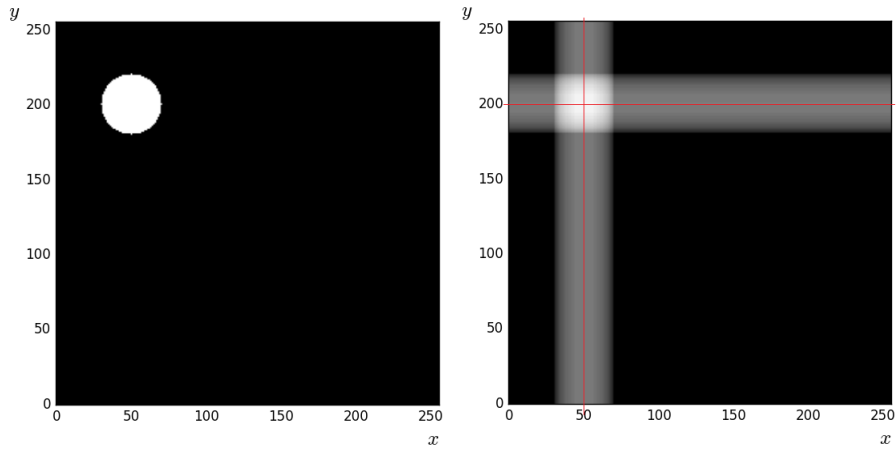
Figure 6: The left image shows the original object. The right image shows the two back projections and the lines along which the center of mass should lie. These lines are shown in red. As can be seen, the intersection is the exact point at which the center of mass of the left image lies.

When this single projection under angle θ is then back projected as discussed in chapter 2.3, the center of mass draws a straight line through the reconstruction. This can be seen in figure 6.

The center of mass of the object will always lie somewhere on that particular line. Adding an extra projection under a different angle will give another line. These lines will intersect somewhere. This intersection is the center of mass of the original object, as it lies on both lines.

So by using at least two projections under different angles, the center of mass of a moving object at a certain time can be obtained. With the previous knowledge, the average velocity of a simple moving object can now be determined in a certain time interval, without knowing the velocity in advance.

Suppose a moving object g is observed and its average velocity $\mathbf{v}_{\text{avg}}$ during a time interval $\Delta t = t$ is calculated using the previous knowledge. In this case, equation 19 holds. The following theorem gives a method of reconstructing the moving object g at $t = 0$ by using only the projections of the moving object.

14

Theorem 3.1.1. *Let g be a moving object and let $f(x,y) = g(x,y,0)$ for all $(x,y) \in \mathbb{R}^2$. Let $\mathbf{v}_{avg} = (v_x, v_y)$ be the average velocity of the object in a time interval $\Delta t = t$. Suppose that equation 19 holds, then the following equality holds*

$$(\mathcal{R}f)(\theta, \rho) = (\mathcal{R}g(\cdot, \cdot, t))(\theta, \rho + v_x t \cos(\theta) + v_y t \sin(\theta)) \tag{22}$$

Proof. First the substitutions $x = x' - v_x \cdot t$ and $y = y' - v_y \cdot t$ are applied to the projections. The idea behind these substitutions follow directly from equation 19. Note that $dx = dx'$ and $dy = dy'$.

$$
\begin{aligned}
(\mathcal{R}f)(\theta, \rho) &= \int_{-\infty}^{\infty} \int_{-\infty}^{\infty} f(x,y)\delta(x\cos(\theta) + y\sin(\theta) - \rho)dxdy \\
&= \int_{-\infty}^{\infty} \int_{-\infty}^{\infty} f(x' - v_x \cdot t, y' - v_y \cdot t)\cdot \\
&\quad \delta((x' - v_x \cdot t)\cos(\theta) + (y' - v_y \cdot t)\sin(\theta) - \rho)dx'dy' \\
&= \int_{-\infty}^{\infty} \int_{-\infty}^{\infty} f(x' - v_x \cdot t, y' - v_y \cdot t)\cdot \\
&\quad \delta(x'\cos(\theta) + y'\sin(\theta) - (\rho + v_x \cdot t\cos(\theta) + v_y \cdot t\sin(\theta)))dx'dy' \\
&= \int_{-\infty}^{\infty} \int_{-\infty}^{\infty} g(x', y', t)\delta(x'\cos(\theta) + y'\sin(\theta) - (\rho + v_x \cdot t\cos(\theta) + v_y \cdot t\sin(\theta)))dx'dy' \\
&= (\mathcal{R}g(\cdot, \cdot, t))(\theta, \rho + v_x \cdot t\cos(\theta) + v_y \cdot t\sin(\theta)),
\end{aligned}
$$

where equation 19 is used in the one but last equality. $\qquad\square$

This means that a simple translation of the projections from the moving object at every time step returns the projections of the stationary object. An example of the application of this theorem can be seen in figure 8. Here a square object is taken and it moves with a constant velocity of $\mathbf{v} = (8, 7)$ pixels per time step. Every time step, two projections under orthogonal angles are taken and these two projections rotate together every step. This is done in such a way, that when all time steps are done, data is gathered over π radians and it is equally spread. This is shown in figure 7. These two projections under different angles are then back projected every step and the center of mass of that image is calculated. The average velocity can be calculated by using these center of masses. This velocity together with the theorem are then applied in the sinogram to obtain a correctly reconstructed, stationary object as can be seen in figure 9.
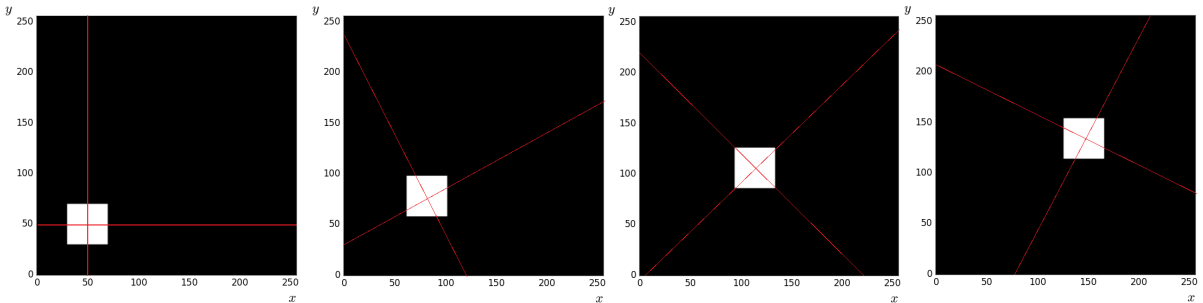

Figure 7: The 4 images show the movement of the object. In every image, two projections are shown and they denote the angle under which the projections are taken. The image are taken at time $t = 0, 4, 8, 12$ respectively and a total of 16 time steps are taken.
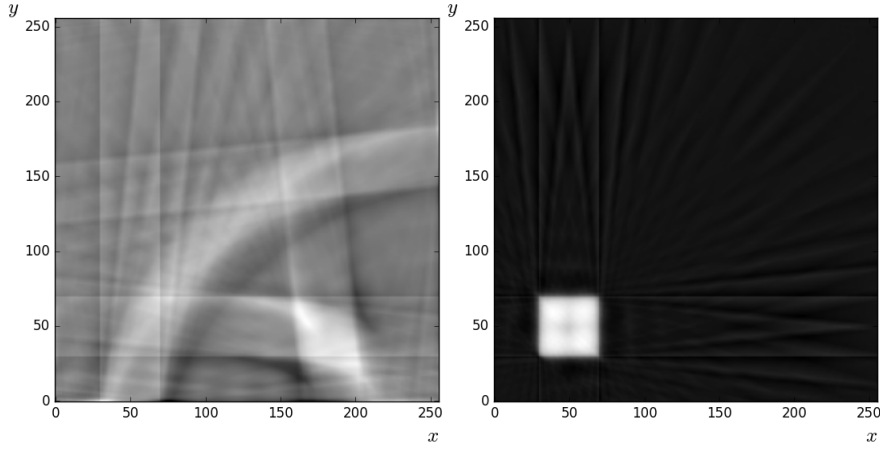
Figure 8: The left image shows the directly reconstructed object, without the application of theorem 3.1.1. The right image shows the correctly reconstructed image after applying the translations in the sinogram. The image is blurry, because of small errors in the calculations and only 32 projections under different angles are taken in total. The image however tells a lot more about the object than the directly reconstructed image. Both images are reconstructed using the SIRT algorithm. For this the ASTRA Toolbox is used.

3.2 Rotating objects

Another type of dynamics is rotation of objects. Especially in the next section this will become useful. In this chapter, the object in question will be a square that rotates. This can be seen in figure 9.
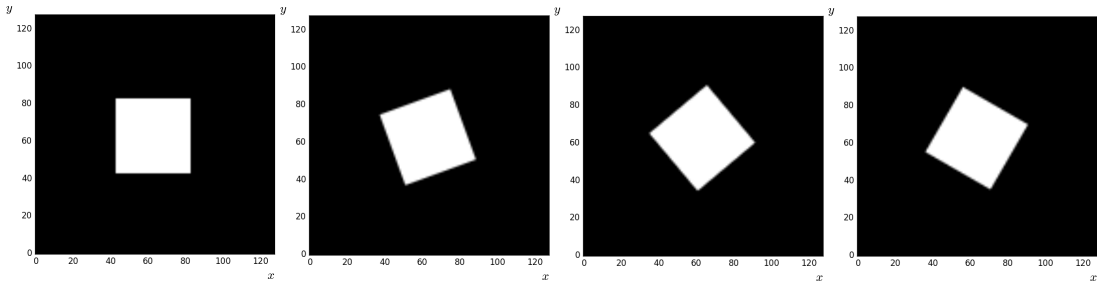

Figure 9: The object rotates counter-clockwise around it's own center . The images are taken at time $t = 0, 10, 20, 30$ respectively.

While this square rotates, a projection under a certain angle is taken. This means that at every time step the angle at which the projection is taken changes, while the object also rotates during that time. The rotation will be counter-clockwise and the angles at which projections are taken also change counter-clockwise. The object rotates 2 times faster than the projection angle. This means that when the projection angles would have finished one period, the object would have rotated two times. The sinogram that belongs to these projections can be seen in the left image in figure 10. When projections are taken from a non rotating square, the results are shown in the right image of figure 10.
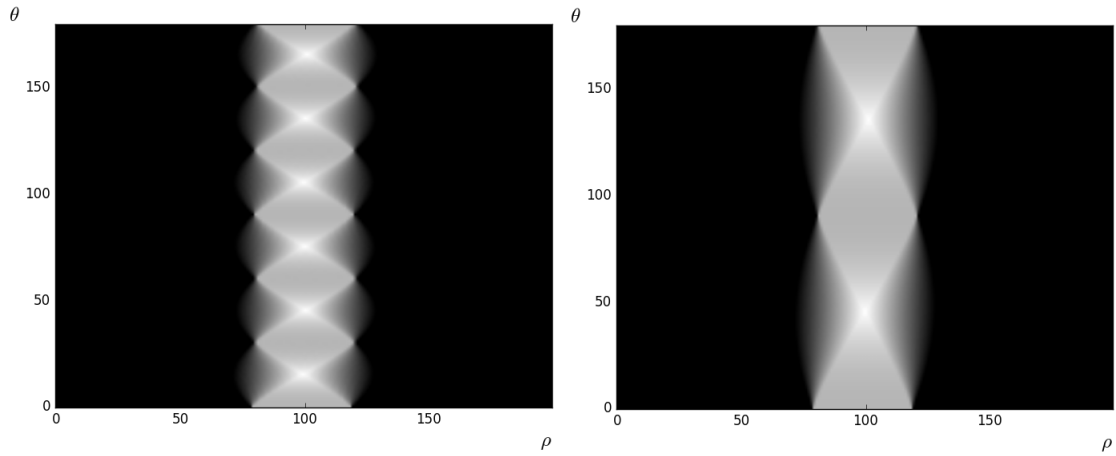
16

Figure 10: The left sinogram is taken from the rotating object in figure 9. The right sinogram is taken from the stationary object, so only the left most image in the same figure. While projections are being taken, the object rotates. This means that before the projections are at the angle $\theta = \pi$, the object has rotated multiple times (in this case two times). So one can see multiple periods of a stationary object in the sinogram of the rotating object.

One can see that multiple rotations of the object, result in multiple periods of the stationary sinogram in the sinogram belonging to the rotating system. Therefore to reconstruct the stationary object, one only needs to take one period in the sinogram belonging to the dynamic system. Only this part should be reconstructed and the result will be a correct stationary reconstruction. This can be seen in figure 11.
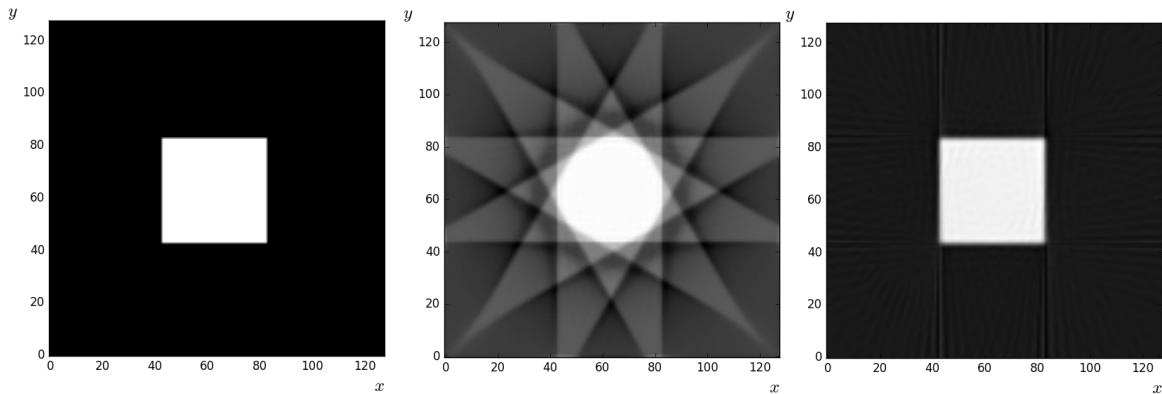

Figure 11: The image on the left is the original object. The goal is to reconstruct this object by cancelling out the rotation. The middle image is the directly reconstructed object from the left sinogram in figure 10. The right image is the correctly reconstructed object, using only one period of the stationary object in the same sinogram.

So there are different methods to negate different types of dynamics in tomography. The next section will discuss the application of these results in astronomy.

4 Astrotomography

In this section the application of tomography in astronomy is discussed. First, a system is introduced on which it can be applied and it is explained how this is done. Then this system is modelled and the data that one would obtain is simulated. Next, the results in the previous section are used to take any rotating movement into account. Last, a method of combining different spectral lines is introduced.

4.1 Cataclysmic Variable stars

To apply tomography, projections are needed of an object, corresponding to different directions. In space this will be a difficult task, as objects are distant and very big. There are however a lot of rotating systems in the universe, where in a certain period of time every side of the object points toward the earth. It is on these types of systems that tomography can be applied, as one can also see the system as being stationary while the earth rotates around it. The main focus of this thesis will lie on Cataclysmic Variable stars, or in short CV. This is a type of binary star where the two stars are so close to each other that matter flows from the lighter star to the heavier one. The heavier, primary star on which this matter accretes is a white dwarf, while the secondary star is called a donor star. The stream mostly consists of hydrogen and the overflow of matter on the white dwarf will form an accretion disc. These accretion discs are the main point of interest for astronomers. The point at which the stream touches the accretion disc is called the bright spot. A schematic overview of this system can be seen in figure 12.
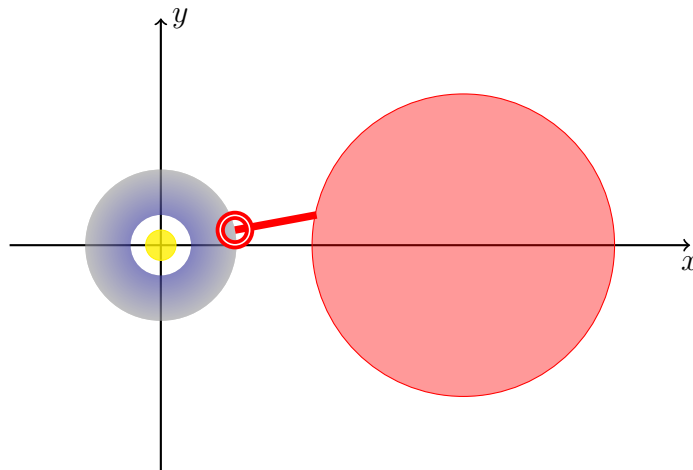

Figure 12: A top down view of a Cataclysmic Variable star. Observations are made perpendicular to this view, so from the side. Mass flows from the donor star (red) to the accretion disc (blue) around the white dwarf (yellow). The point that the stream touches the disc is called the bright spot. The colours are not representative to the real colours that these elements are.

Unfortunately, CV systems are so far away that current telescopes are not able to directly image them. This will make the application of tomography difficult. However, there is another way to observe these systems. The main observation technique used is spectroscopy. Here, one measures how much light (flux) is received for different wavelengths of light. This is done by using filters that only let through light of that particular wavelength in the telescope. The main point of interest in these spectroscopic images lies around emission lines of hydrogen and helium.

Emission lines of a certain atom are specific wavelengths at which the atom sends out light when an electron changes from energy shell. Different changes in energy of the electron result

in different emission lines for the same atom. So every atom has multiple emission lines. Note that these emission lines are unique for every different type of atom. So a hydrogen atom for example has completely different emission lines than a helium atom. The wavelengths at which these emission lines occur are known as these can be calculated mathematically. So if a peak in flux is seen at an emission line of for example hydrogen, it indicates that hydrogen is present in the object that is observed. An example of a few emission lines of hydrogen can be seen in figure 13.
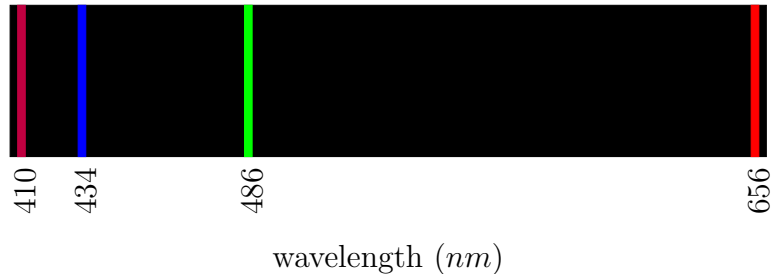

wavelength (nm)

Figure 13: An example of emission lines of hydrogen. Hydrogen has more emission lines, but the ones shown are in the visible light (the colours humans can see). These are lines that are part of the so called Balmer lines.

The main point of interest for astronomers is the structure of the accretion disc and what substance this disc is made of. A way to know if a certain type of atom lies in the disc (and not the star) is the Doppler effect of light. When a source sends out light at a particular wavelength and moves at high speed away from (towards) earth, the wavelength observed will be bigger (smaller) than the emitted wavelength. The light is redshifted (blueshifted). This is equivalent to the Doppler effect with sound. The accretion disc rotates at very high speeds and therefore part of the disc will seem to move away from earth, while the other side moves towards it. This results in two shifted peaks in the spectroscopic image, one to the right of the emission line and one to the left. The inner part of the disc rotates the fastest and also emits the most light, while the outer part rotates slower and emits less light. So it is expected to get a peak in flux at high absolute radial velocities, because more flux comes from elements moving at high speeds away or towards us. By convention, radial velocity is defined as the velocity component pointed away from earth. The total flux coming from particles decreases when the absolute radial velocity decreases, by reasons just mentioned. This results in many possible shapes of the spectroscopic data, but the two peaks at high absolute radial velocities are always visible. An example of how a spectroscopic image could look like, can be seen in figure 14.

In figure 14, the flux is measured per wavelength. However, the Doppler effect can correlate a shift in wavelength directly to a radial velocity. This is done using the following formula.

$$v_R = c \cdot \frac{\lambda_{\text{obs}}^2 - \lambda_{\text{emit}}^2}{\lambda_{\text{obs}}^2 + \lambda_{\text{emit}}^2}, \tag{23}$$

where v_R is the radial velocity, c is the speed of light, λ_{obs} is the observed wavelength and λ_{emit} is the emission line wavelength (emitted wavelength). With this, the flux at different wavelengths can be expressed as the total flux coming from all particles with a certain radial velocity. This will be used for tomography to be applied.

One could take these observations at different points in time, to obtain data from different sides (orbital phases) of the CV. In the next chapter it will be shown that this data can be seen as a projection and by combining these images under different angles a sinogram is obtained which can be reconstructed.
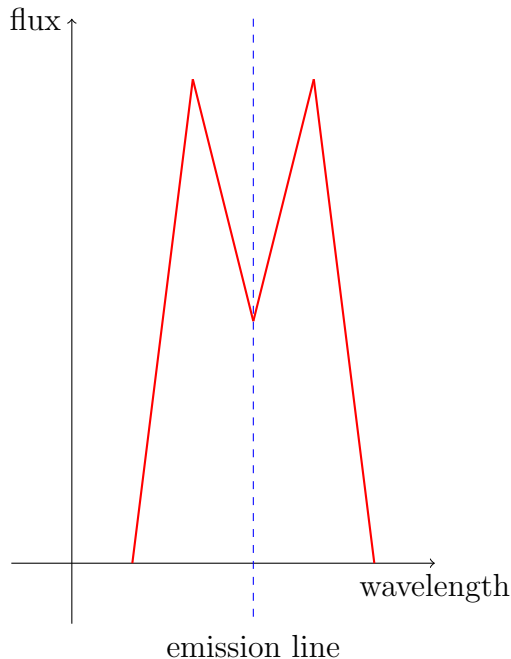
Figure 14: Schematic graph of the spectroscopic data from a CV. Two peaks are seen left and right of the emission line. The left one is blueshifted, which belongs to the part of the disc that rotates towards earth. The right one is redshifted, which belongs to the part of the disc that rotates away from earth

4.2 Tomographic set-up

In this chapter the tomographic set up will be discussed. Most of the content is also described in [2].

   The data that is obtained during observations results in the total flux from all particles with a certain radial velocity. This radial velocity can therefore be compared to the variable ρ in section 2. The difference will be the line along which this is integrated. This can be understood by looking at figure 12. It is convention to let the x-axis point from the white dwarf to the donor star and the y-axis point to the direction the donor star moves. The system rotates and this rotation will be defined by the angle $\phi \in [0, 2\pi)$. Note that astronomers define orbital phase as $\frac{\phi}{2\pi}$. This term will be used often in this thesis and gives the fraction of the total period. $\phi = 0$ is defined as the moment that the donor star is in front of the white dwarf. The donor star moves at first in the direction of positive y. This can also be seen as the system being stationary and the earth moving around, first in the direction of negative y. This is also the direction at which we let our ϕ increase. The radial velocity (v_r) is defined as the velocity away from us. With these conventions, the following equation holds:

$$v_r = \gamma - v_x \cos(\phi) + v_y \sin(\phi). \tag{24}$$

Here, γ is the velocity at which the whole system moves away from us and v_x and v_y are the velocities in the x and y direction respectively. As discussed before, the data is the total flux coming from particles with a certain radial velocity. This means that this can be seen as an integration of flux along the line in equation 24. So one spectroscopic image taken at angle ϕ can be seen as a projection under angle ϕ. The theory in section 2 can then be applied, but with different coordinates. Reconstruction will therefore obtain the flux coming from all particles with a specific v_x and v_y. This will be called a Doppler diagram or velocity diagram.

20

4.3   Problems

There are a few problems concerning the application of the theory to astronomic sources. These are not the only problems, but they are the ones that are most problematic.

1. Not all parts of the system are equally visible from earth.

2. The flux from parts of the system can vary in time.

3. Not all motion in the system has to be parallel to the orbital plane.

4. Doppler diagrams can not be uniquely coupled to a spatial model of the accretion disc.

An example of an occurrence of the first problem is that only the outer layer of the stars are visible from earth. The inner regions give of light, but it is scattered so much that one can not distinguish where the light comes from. This clearly violates one of the assumptions of tomography.

The second problem can be understood by looking at the sun and its sunspots. These sunspots change the amount of light emitted from that particular region, but they also vary in size over time. This means that the flux coming from parts of the stars will not be constant.

When motion is not parallel to the orbital plane, the velocities that are measured are projections of the actual velocities. Therefore the reconstructed image will not give a correct image of the actual system, but a projected one. These systems are not directly observable, so one can not check if all motion is parallel to the orbital plane.

The last problem mentioned in this thesis concerns the Doppler diagrams. These diagrams are given in velocity coordinates, but they are hard to couple to spatial coordinates. Moreover the coupling of these diagrams to models of the system in spatial coordinates is not unique, as different models can be taken for the velocity coordinates and for the intensity profile of the disc, while the Doppler diagrams of these models could be equal. This last problem is less of an issue than one could think. Some models are more probable than others as they have to follow certain physical laws. However, not much research is done about the coupling of Doppler diagrams to models.

In the following chapter, Doppler diagrams and the data that would be obtained are simulated for certain CV models.

4.4   Simulator

It is difficult to connect a Doppler map to a certain model of an accretion disc. Therefore it is necessary to do simulations on these maps using different models of accretion discs. These simulations can then provide a probable model to the obtained data. There is no guarantee that the accretion disc behaves like the models used in this thesis, but they are the most probable models according to the current understanding of CV's.

For the simulations python is used and for the application of tomography to these models, the Astra toolbox is used. The input will be a model of an accretion disc, containing the intensity and the velocity in the x and y directions of the disc at every pixel. It will return the data that would be obtained if one would observe a CV with that particular accretion disc, which is a sinogram of the combined spectral data. The first and most probable model for the disc is a homogeneous disc. The atoms that are modelled could be hydrogen or helium and the flux could be of any spectral line of these two atoms. The white dwarf and the bright spot have been left out, as they are of no interest and can easily be spotted in the data. The intensity profile is taken to be proportional to the square root of the radius. The velocities are modelled as Kepler velocities. This means that they also are proportional to the square root of the radius

and have a direction orthogonal to the position vector in the direction of the discs rotation, which is counter-clockwise with the chosen axes. The size of the disc is less relevant, as the system can be scaled to obtain correct sizes. In this thesis, the size is counted by pixel values and can therefore be transformed relatively simple to actual values. However, the velocities in the model are chosen to be somewhat realistic if one multiplies every component with 10^3. It then has units of km/s. A more detailed explanation of the realism of this model can be found in section 5. A Doppler map is calculated during the creation of this model. The Doppler map is a 40×40 pixel array, where each pixel corresponds to a certain velocity range $v_x + dv_x$ and $v_y + dv_y$. While the model is created and the v_x and v_y velocities are assigned to each pixel, it is checked in what pixel of the Doppler map that particular velocity belongs. The intensity of that pixel in the model is then added to the pixel value in the Doppler map. Using this method, both the model and Doppler map are created at the same time. Afterwards, 360 projections with a total of 60 pixels at different angles are taken from this Doppler map to obtain the data that would be observed. These projections are evenly spread around one orbital phase. The projections are taken using the ASTRA Toolbox, which has a function that takes projections of an input array and returns the sinogram. The results can be found in figure 15. The v_r axis in the sinogram has to be taken lightly. The numbers correspond to pixel values and are not actual velocities. The numbers have been taken in such a way that zero is in the middle, as this is the part of the data that has zero radial velocity. To obtain actual velocities, one should calculate the radial velocity belonging to every projection taken of the Doppler map. However, in this thesis the shape of this diagram is of bigger importance. This is the reason why the pixel values are shown. Note that in astronomy, the color map used for these images is inverted, so white means no flux and the darker the pixel the more flux is coming from it.
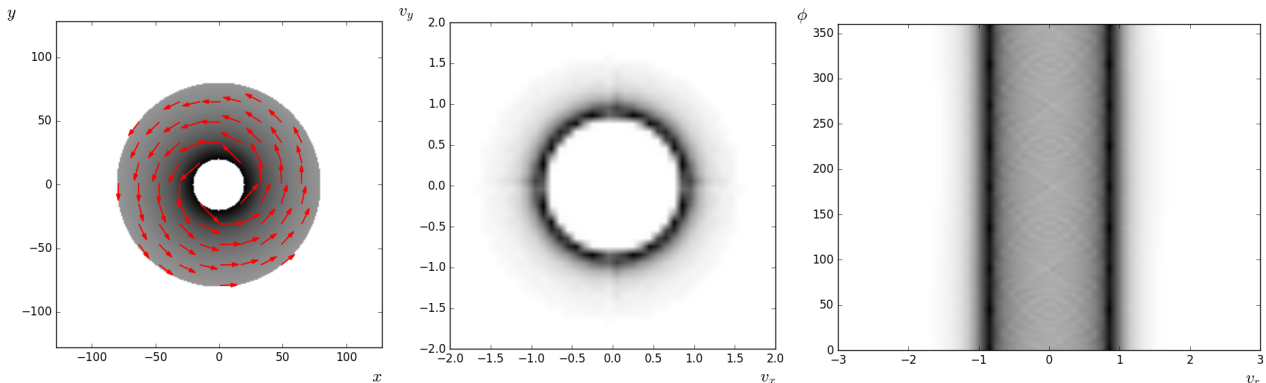

Figure 15: The left images shows the model that is used. The arrows indicate the relative size and direction of the velocities. The middle image is the Doppler map belonging to the model. The right image is the sinogram belonging to the Doppler map. This represents the data obtained from a system that behaves like the model.

The data that would be obtained looks similar to actual data that can be found in the chapter "Mapping the Peculiar Binary GP Com" in [2]. The only thing that is different, is the sinusoid in the data that is caused by the bright spot. However, this is missing in the model data, because the bright spot was not put in the model. The Doppler map is completely symmetrical, which follows directly from the symmetry in the velocities. It is good to note that the inner parts of the accretion disc rotate at higher speeds. This means they can be seen on the outer parts of the Doppler map. So the disc will be seen as if it is inside out.

A more interesting case is when the accretion disc has a more interesting structure. Previous research, such as "Spiral Waves in Accretion Discs - Observations" in [2], suggests that there might be accretion discs with a spiral pattern. This gives a non-homogeneous pattern and

results in more interesting and peculiar data. The model used and the resulting data can be seen in figure 16
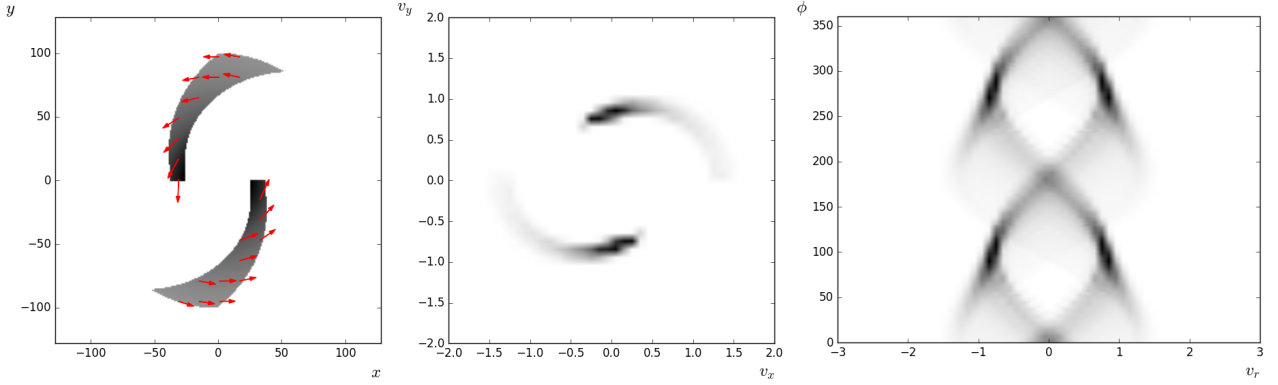

Figure 16: The left images again shows the model that is used. The arrows indicate the relative size and direction of the velocities. The middle image is the Doppler map belonging to the model. The right image is the data that would be obtained from a system behaving as our model.

Each spiral in the model in figure 16 was made using the spiral formula

$$r = a + b\theta^2 \tag{25}$$

where r is the radius, θ the angle and a and b are constants. a denotes the starting point of the spiral and b denotes the distance between following turns. These constants are chosen in such a way to obtain a realistic model of a spiral disc. Although not much is known about these discs, the shape probably looks like the model. The doppler map still has symmetry in it, but it is no longer a closed disc, as there are holes between the spirals of our model. The sinogram is more interesting, as one can clearly see characteristics of a spiral. Under a certain angle both arms will be equally visible, but as the system rotates there will come a point in time where the spirals are behind each other. So the arms in the sinogram will come together, after which they will separate again. Two periods can be seen, as the measurements are taken during one orbital phase and as discussed in section 2 one only needs π radians of data as the other π radians will just be mirrored. The spiral characteristics in the data can also be seen in actual data found in [2].

In the cases above, a static model was used and the velocity vectors denote the rotation of the complete system. One could however imagine that such a system has more internal dynamics. The disc for example could rotate at different speeds than the whole system. This would give distorted data. In the following chapter, dynamics where added to the model.

4.5 Adding rotation to the accretion disc

Rotation was added to each of the models discussed in the previous section. A rotation in the model also rotates the velocity vectors. This means that a rotation in the model corresponds to the same rotation in the Doppler diagram. As the calculation of the Doppler diagram is rather slow, the rotations were performed on the Doppler map instead of the model. Every time step, the Doppler map was rotated and a projection was taken under the angle belonging to that time step. The rotation was done by applying the inverse rotation matrix on every pixel in the rotated diagram. This gave the original coordinate before rotation and the pixel value in that pixel was used for the rotated coordinate. When the coordinate lay in between pixels, interpolation was used.

When using the model in 15 and adding rotation to it, nothing changed. The shapes where exactly the same as in that figure. This is understandable, as the disc is completely symmetric and so are the velocities. So a rotation does not change the image and therefore not the projection taken at every time step.
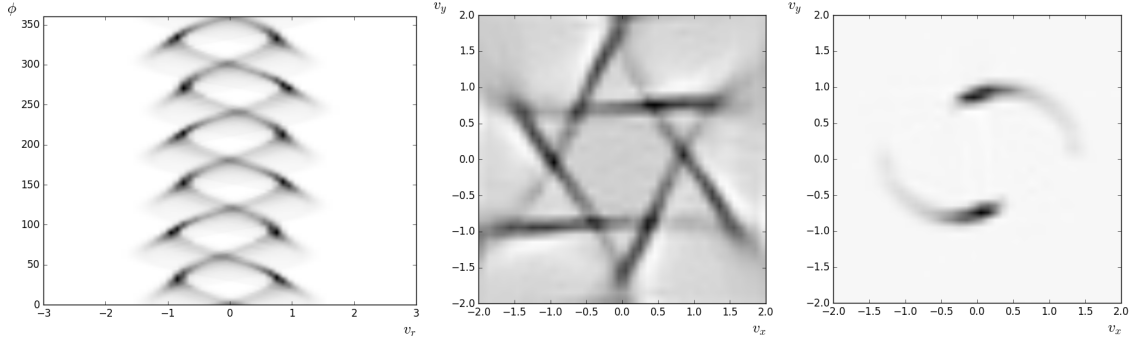

Figure 17: The left images shows the data that would be obtained if one would use the model in figure 16 and let it rotate at twice the speed the system rotates. The middle image shows a direct reconstruction from the data. The right image shows a correct reconstruction of the data by using the method described in section 3.2. The reconstructions are again done by using the SIRT algorithm in the ASTRA Toolbox.

In figure 17, one can see the data belonging to the model as in figure 16, but with added rotation. This rotation will be in such a way that the disc rotates two times in one orbital phase of the system. Next to the data shows the directly reconstructed image of the data without taking into account the rotation. The right image shows the correctly reconstructed image using the method described in section 3.2. Comparing that image to the Doppler diagram belonging to the stationary model in figure 16, one can see that the dynamics of the disc are cancelled out as expected.

If one calls k the amount of rotations of the accretion disc in one orbital period, then the amount of periods in the data is equal to $(k + 1) \cdot 2$. The 2 follows from the result found in section 2, where it was found that only π radians of data is needed, while in the image data is obtained in the full orbital period. The added one to the constant follows from the changing of the angle during the projections. When the system does not rotate while the disc does, one would see k rotations. However, during this time the complete system also has one rotation. This explains the $k + 1$. So from the data, one can find how much faster the disc rotates in comparison to the whole system.

One problem is, that most of the found systems have a homogeneous disc. Therefore it would be of value if one could find asymmetry in these systems. If asymmetry is found in the system, it can be confirmed by looking at more spectral lines of the same atom. However, spectral lines often overlap and one can not reconstruct this overlapping spectroscopic data directly. In the next chapter a method is proposed for the reconstruction of overlapping spectral data.

4.6 Combining spectral lines in reconstruction

The previous results are obtained by using a spectral line that is not close to any other spectral lines of hydrogen or helium. There are however some lines that lie close enough together for the patterns in the sinogram to overlap. Normal reconstruction is not possible on these sections of the spectroscopic data, as a different spectral line results in it's own sinogram. It could however be useful to reconstruct the overlapping spectral lines if one wants to confirm results found at other spectral lines. In this section the mathematics behind the overlap is discussed

and it is shown that the problem can be written in the shape of equation 15 and can therefore be reconstructed. This would result in an individual Doppler diagram for both spectral lines. At the end of the chapter the theory is applied and correct reconstructions will follow from model data of combined spectral lines.

4.6.1 Theory

The first spectral line will be called X and the second one will be called Y. The wavelength difference between the two spectral lines is given by ϵ. As was discussed in chapter 2.4, the reconstruction problem of the two individual spectral lines can be written as

$$\mathbf{W}\mathbf{V_X} = \mathbf{P_X} \qquad\qquad \mathbf{W}\mathbf{V_Y} = \mathbf{P_Y} \tag{26}$$

where $\mathbf{W}$ is an $M \times N$ weight matrix, $\mathbf{V_X}$ is the vector of length N containing the Doppler diagram belonging to spectral line X, that is ordered as discussed in chapter 2.4 and $\mathbf{P_X}$ is the projection data with length M. The variables with the Y subscript belong the spectral line Y. The linear equations both contain the same weight matrix as they both have the same projection set-up.

When the projection data is seen as a sinogram, the actual data of one of the spectral lines would be shifted, as compared to the other spectral line. This is because there is a difference ϵ between the emitted wavelengths and each line corresponds to a radial velocity of zero. One can couple this shift in wavelength to a shift in pixels in the diagram, depending on how many pixels correspond to a change in one wavelength. From now on without loss of generality, it is assumed that $\mathbf{P_Y}$ is shifted $s \in \mathbb{N}$ pixels in the total combined sinogram in the direction of increasing wavelength.

Suppose that the sinogram consists of $m_1 \cdot m_2 = M$ pixels, where m_1 is the amount of rows and m_2 is the amount of columns. Then this data can be put in a vector as explained in chapter 2.4. A shift of s pixels then comes down to multiplying the projection data with the following $M \times M$ matrix

$$\mathbf{D} = \begin{pmatrix} \tilde{\mathbf{D}} & \mathbf{0} & \cdots & \mathbf{0} & \mathbf{0} \\ \mathbf{0} & \tilde{\mathbf{D}} & \cdots & \mathbf{0} & \mathbf{0} \\ \vdots & \vdots & \ddots & \vdots & \vdots \\ \mathbf{0} & \mathbf{0} & \cdots & \tilde{\mathbf{D}} & \mathbf{0} \\ \mathbf{0} & \mathbf{0} & \cdots & \mathbf{0} & \tilde{\mathbf{D}} \end{pmatrix} \tag{27}$$

of $m_1 \times m_1$ sub matrices that are either the zero matrix or $\tilde{\mathbf{D}}$. $\tilde{\mathbf{D}}$ is an $m_2 \times m_2$ matrix that has the form

$$\tilde{D}_{ij} = \begin{cases} 1, & \text{when } i = (j + s) \bmod m_2 \\ 0, & \text{else.} \end{cases} \tag{28}$$

This is just the identity matrix where the columns are shifted by s entries to the right. The matrix D has that particular shape because of the way the pixels of the sinogram are ordered in the projection data. The actual data received is then the summation of both projection data, but with the shift in the projection data for spectral line Y. When the equations in 26 are used, the following system of linear equations forms

$$\mathbf{P_X} + \mathbf{D}\mathbf{P_Y} = \mathbf{W}\mathbf{V_X} + \mathbf{D}\mathbf{W}\mathbf{V_Y} = \begin{pmatrix} \mathbf{W} & \mathbf{D}\mathbf{W} \end{pmatrix} \begin{pmatrix} \mathbf{V_X} \\ \mathbf{V_Y} \end{pmatrix} \tag{29}$$

This equation closely resembles equation 15. It says that the total projection data is equal to the matrix containing the weight matrices as sub-matrices next to each other, multiplied by the vector containing both velocity diagrams. As these are linear equations, they can be solved using reconstruction algorithms.

4.6.2 Application

Because the weight matrix has to be adjusted for correct reconstruction, the ASTRA Toolbox can not be used. It does not support any changes to the calculated weight matrices. Therefore the SIRT reconstruction technique was used manually. The original weight matrix $\mathbf{W}$ was calculated by using the ASTRA Toolbox with the desired projection set up. This projection set up will be a total of 60 projections over π radians, with 40 pixels per projection. This results in a total of $M = 40 \cdot 60 = 2400$ entries for the projection data. One Doppler diagram is 1600 pixels, so the combined diagrams are $N = 3200$ pixels. This gives a total combined weight matrix of 2400×3200 pixels. This is relatively small and this matrix can be calculated directly. The ASTRA Toolbox can only calculate the matrix W, not the combined matrix. Therefore W was read out and the correct changes were made to obtain the combined weight matrix. The matrix W could also be calculated manually [9]. Also note that the total system of equations will be under determined, as $M < N$. Because in this case more solutions are possible, a method of obtaining the wanted solution from the reconstruction will also be given.

Model data is created by using the model in the left most image of figure 16 for substance X and the model in the left most image of figure 15 for substance Y. This is not a realistic model, as often different atoms still have the same distribution in the disc as can be seen in results found in [2]. However, this model is chosen for testing purposes. The simulated data in the same figures is used and the data of Y is shifted 5 pixels to the right. In figure 18 the used models and the model data can be seen. The shift of 5 pixels is chosen for simplicity, in normal situations one should base this shift on the difference between spectral lines as discussed previously.
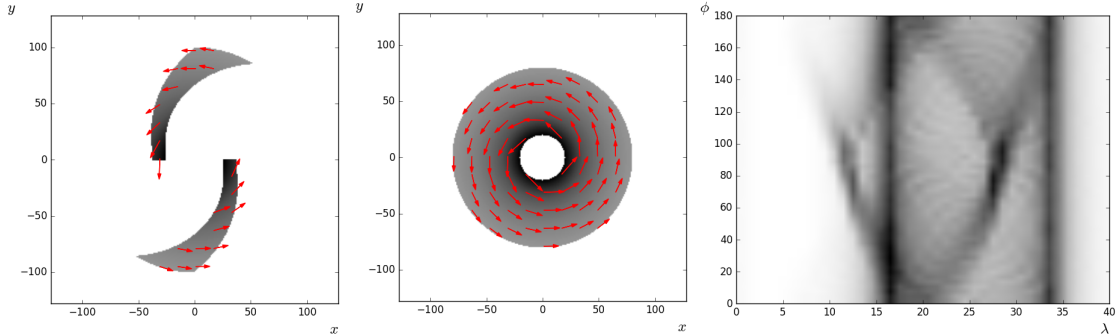

Figure 18: The left image shows the model used for X and the middle image shows the model used for Y. Doppler images and data belonging to these models are calculated as done in chapter 4.4. The data of Y is shifted by 5 pixels and then combined with X. This results in the model data shown in the right image. The λ axis simulates wavelength, because velocities can not yet be coupled as two spectral lines are used.

With the model data and the combined weight matrices, a reconstruction can be made. The SIRT algorithm is used for this with 500 iterations. At first, an initial condition of $\mathbf{x}^{(0)} = \mathbf{0}$ was used. This resulted in an unwanted solution for the diagrams, so a different starting condition has to be used. If one already obtained Doppler diagrams from the atoms of X and Y at other spectral lines, these can be used as initial conditions. These should also approximately be the solutions to the combined spectral data. If this is not available, one should guess the approximate shape of these diagrams based on the overlapping data. In this thesis, the Doppler diagrams of other spectral lines of X and Y were simulated and used. For atom X the Doppler map is used in figure 16 and for atom Y the Doppler map is used in figure 15. Using these starting conditions for $\mathbf{x}^{(0)}$, the correct reconstructions follow as can be seen in figure 19.
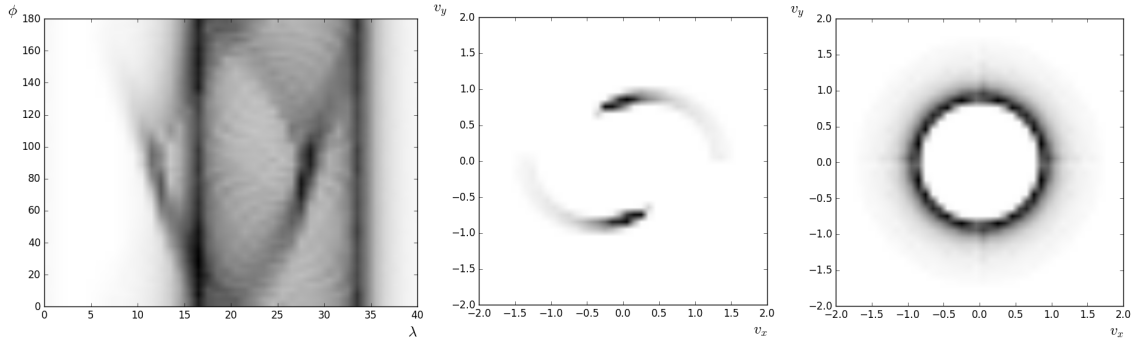
Figure 19: The left image shows the model data of the combined spectra, the middle image shows the reconstruction of X and the right image shows the reconstruction of Y. These are both reconstructed at the same time from the data using SIRT.

In this case the wanted reconstructions are the same as the initial conditions and it is only natural that SIRT then converges to that solution. In a more practical scenario, the Doppler maps used as initial conditions differ from the to be reconstructed ones. They are however similar to the to be reconstructed Doppler maps as they are of the same atoms. When no other spectral data is available for the atoms of X and Y, one could make models of X and Y as done in chapter 4.4. The Doppler maps could then be calculated and used as initial conditions of SIRT. This could result in a correct reconstruction if the correct model was chosen.

5 Conclusion

In this thesis, the basic analytical and algebraic set-up of tomography was described. Some analytical reconstruction methods were explained, along with an algebraic one and a measure was given to check the quality of these reconstructions. Methods of cancelling out simple and rotational dynamics were given. The correction of simple dynamics followed directly from the mathematics described in chapter 2. However, the velocity of the object was needed at every time step. This could be measured by taking at least two projections from different angles of the object at every time step. It was also shown that rotational dynamics could be corrected, by only reconstructing part of the data. The basic set-up for astrotomography was described. Different types of models were made of the accretion disc of Cataclysmic Variable stars and the data that would be obtained from these systems was simulated. The method of cancelling out rotational dynamics was used to correct any possible dynamics in the disc. Finally, a method was given to reconstruct overlapping spectroscopic data.

One downside to the method of correcting simple dynamics, is the need of two projections from different angles of the object at every time step as this is not always possible. However, when one knows the velocity of the object the method can still be applied to any data obtained from a moving object. The method proposed for correcting rotational dynamics is an empirical result and should be mathematically confirmed in future research, which should not be too difficult.

The models used for the accretion disc are simplified and assumptions were made on the velocity model en the intensity profile of the disc. The velocity model used is the primary candidate of the correct model for the system, however the light profile was a choice that could not be supported by previous research. It was taken based on the comparison between the simulated data and realistic data by eye. To improve this model, the light profile could be fitted to actual data. This can be done by simulating the data of different profiles and measuring the similarity between this simulated data and actual data by using the RRMSE measure. The same can be done for the model of the spiral disc.

The addition of dynamics to the accretion disc is also not supported by previous research. Up until now, no data confirms that there are systems where the accretion disc has a different rotational period than the whole system. The results however can be directly applied if such a system would be found.

The results of the reconstruction of combined data are useful if one has an idea of the Doppler maps that are to be reconstructed. One could improve the convergence of SIRT to the wanted reconstruction by taking more projections. Only SIRT was tested for the reconstruction. In the future, one could try other algorithms that are better at reconstructing under determined systems.

References

[1] G. van Eyndhoven, K.J. Batenburg, D.Kazantsev, V. van Nieuwenhove, P.D. Lee, K.J. Dobson, and J. Sijbers. An iterative ct reconstruction algorithm for fast fluid flow imaging. *IEEE Transactions on Image Processing*, 24, 2015. doi: 10.1109/TIP.2015.2466113.

[2] H.M.J. Boffin, D. Steeghs, and J. Cuypers. *Astrotomography*. Springer-Verlag Berlin Heidelberg, 2001.

[3] F. Natterer and F. Wübbeling. *Mathematical Methods in Image Reconstruction*. Society for Industrial and Applied Mathematics, 2001.

[4] W. van Aarle, W.J. Palenstijn, J. de Beenhouwer, T. Altantzis, S. Bals, K.J. Batenburg, and J. Sijbers. The astra toolbox: A platform for advanced algorithm development in electron tomography. *Ultramicroscopy*, 157:35–47, 2015. doi: 10.1016/j.ultramic.2015.05.002.

[5] W. van Aarle, W.J. Palenstijn, J. Cant, E. Janssens, F. Bleichrodt, A. Dabravolski, J. de Beenhouwer, K.J. Batenburg, and J. Sijbers. Fast and flexible x-ray tomography using the astra toolbox. *Optics Express*, 24:25129–25147, 2016. doi: 10.1364/OE.24.025129.

[6] Xavier Saint Raymond. *Elementary Introduction to the Theory of Pseudodifferential Operators*. CRC Press, 1991.

[7] E.M. Stein and R. Shakarchi. *Fourier Analysis: An Introduction*. Princeton University Press, 2003.

[8] J.S. Jørgensen. Introduction to tomographic reconstruction. `http://www2.compute.dtu.dk/~pcha/HDtomo/SC/Week1Days1and2.pdf`, January 2017. Accessed: February 21, 2017.

[9] G. Han, Z. Liang, and J. You. A fast ray-tracing technique for tct and ect studies. *IEEE Nuclear Science Symposium, 1999. Conference Record*, 3:1515–1518, 1999. doi: 10.1109/NSSMIC.1999.842846.